X-ray Photoelectron Spectroscopy (XPS)

Jacopo Venturin Timo Dully Nereu Montserrat i Busquets

Tutor: Rahil Hosseinifar

May, 30, 2023

Abstract

X-ray Photoelectron Spectroscopy (or XPS) is a common technique used to analyze the electronic composition of material samples. It is based on the photoelectric effect and makes use of different sources of $X-$ray radiation - in our case we can employ either an Al or a Mg anodes. During XPS the kinetic energy of electrons emitted by the material through photoelectric effect is detected and used to identify the electronic profile of the sample.

However the binding energy is not the only relevant effect on XPS and thus one may also observe effects due to electronic relaxation and changes in shell composition such as Auger peaks, shake-up and shake-off. We will use XPS to analyze three samples (Ag, Sm and a Coin) and distinguish the 3p and 3d peaks of the main components. We also observe orbital splitting due to spin-orbit interactions and compute the spin-orbit coupling constant.

1 Introduction

The interaction between radiation and matter can take place in different ways. The main ones are **diffusion**, through elastic or inelastic scattering, and **absorption**, with or without consequent emission of a photoelectron. This effect was first described by Hertz in 1887, and then was theoretically explained by Einstein in the 1905 considering the quantum nature of light [3].

The energy of the incident photon can be in the ultraviolet regime ($5 - 100\,\text{eV}$), the soft X-ray regime ($100 - 1000\,\text{eV}$) or the X-ray regime ($> 1000\,\text{eV}$). In the latter case, we speak of X-ray Photoelectron Spectroscopy or abbreviated XPS [3]. The XPS method was developed by Kai Siegbahn (Nobel Prize in Physics 1981), using Al-K_α and Mg-K_α, with energies 1486.7 eV and 1253.6 eV respectively [1].

XPS allow, by measuring the kinetic energy of the emitted photoelectron, to get information about the electronic shell structure of the material of interest.

An important feature of XPS is that it is a particularly surface sensitive technique. This implies that photoelectrons are emitted only from a thin layer on the surface of the material being analyzed. In particular, it is possible to achieve with XPS a depth of escape λ between 2 Å and 20 Å, depending on the kinetic energy [1].

.

2 Theory

The main process we are interested in during an XPS experiment, is the photoelectron emission due to the absorption of a photon with energy $E_p = h\nu$, where h is the Planck constant and ν is the frequency. If the incident photon has enough energy to overcame the vacuum energy level, the electron is ejected from the atom with a final kinetic energy E_{kin}.

For this process we can write down an equation associated to the energy conservation for a single atom A:

$$E_A^{(i)} + h\nu = E_A^{(f)} + E_{kin} + \Phi, \tag{1}$$

where $E_A^{(i)}$ and $E_A^{(f)}$ are the energy of the atom before and after the absorption of the photon respectively, E_{kin} is the kinetic energy of the emitted photon and Φ is the work function. This latter is characteristic of the material we consider and quantify the energy difference between the *Fermi level* and the vacuum level (see Fig. 1).

Fermi level is a concept coming from the Fermi-Dirac statistics, used to describe fermions, and in particular electron. If we consider a single electron at 0 K, it's maximum energy corresponds to the so called Fermi energy. Because of the Pauli's exclusion principle, two different electron cannot exist at the same time in the same state. This implies that the energy states of different electrons must be arranged on top of each other so as to minimize the energy of the system. The highest energy state is called the Fermi level. Using the Fermi level μ it is possible to show, via the Fermi-Dirac statistic, that the probability of occupation of a level with energy E by an electron is given by the Fermi function

$$f(E) = \frac{1}{1 + e^{\beta(E-\mu)}},$$

where β is the reciprocal of the product between the Boltzmann constant K_B and the temperature T.

2.1 Binding energy

The energy difference between the final and the initial state of the atom is known as **binding energy** and it is referred as

$$E_B = E_A^{(f)} - E_A^{(i)}.$$

In this equation the binding energy is computed respect to the Fermi level, but in principle that can be also expressed relative to a different reference level. For example in gas phase photoemission binding energies are measured from the vacuum level, while in the study of solids, the Fermi level is used as a reference[2].

Using the definition above we can rewrite the equation (1) as

$$E_{kin} = h\nu - E_B - \Phi. \tag{2}$$

From equation (2) it is clear that the binding energy of all core electrons with energy lower than $h\nu + \Phi$ (assuming the Fermi level as a reference for the binding energy) can be determined.

Equation (2) also shows that, with the same frequency of the X-ray incident on the sample, a higher kinetic energy will be transmitted to photoelectrons with lower binding energy. For example, the peaks associated with valence electrons will have a lower kinetic energy than that of the core electrons.

In practice, a measure of the binding energy will always present, in addition to the contribution of the individual atom, also contributions that are due to the multi-body nature of the

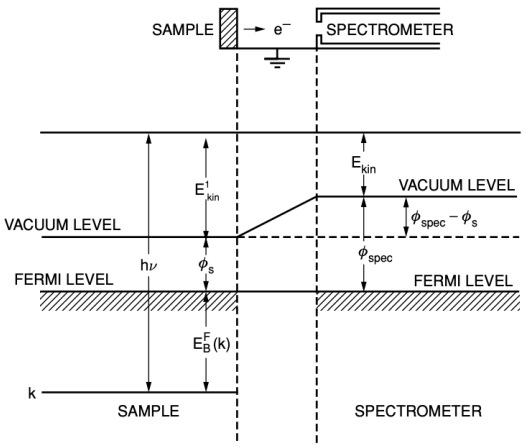

Figure 1: Different energetic contributions for the measurement. In this picture the sample and the spectrometer have the same Fermi level, since they are in electrical contact. The kinetic energy detected by the spectrometer is $E_{kin} = E^1_{kin} - \Phi_{spec} + \Phi_s$. Picture taken from [2]

sample we are using to perform the measure. In particular we can see the binding energy for a material as a sum of different contributions:

$$E_B = E_B^{Atom} + \Delta E_{chem} + \Delta E_{Mad} + \Delta E_{rel} \tag{3}$$

where ΔE_{chem} is the chemical shift due to the effect of chemical bonds, ΔE_{Mad} is the Madelung constant that is associated to the electrostatic energy of the solid lattice, while ΔE_{rel} takes care of the 1-hole final state of the investigated many-body object [1].

2.2 Surface sensitivity

An important aspect of XPS measurements is the surface sensitivity. In general a technique that is particularly surface sensitive should allow to measure up to one monolayer of sample without signal from the bulk under it. A fundamental quantity to describe the surface sensitivity is the mean escape depth λ of a photoelectron. A lower λ corresponds to higher surface sensitivity. The mean escape depth as a function of the energy of the photoelectron is the so called *universal curve of escape depth* (see Fig. 2). XPS turns out to be particularly surface sensitive for kinetic energy in the range $20\,\text{eV} - 100\,\text{eV}$, allowing measurements up to 1 monolayer [1].

2.3 Secondary electrons

In addition to the emissions associated with the core and the valence bonds electrons, other types of excitation processes are present in solids:

- **Auger processes**: as the X-rays strike the sample, Auger electron emission can occur. This process is due to the presence of excited ions formed as a result of the emission of a core electron. When an outer electron fills the inner shell, a photon is emitted. If the emitted photon interacts with another electron this can be ejected from the atom.
- **Energy losses in inelastic scattering**: is the origin of the inelastic scattering tail, that corresponds to a smooth pick with lower kinetic energy compared to the main pick

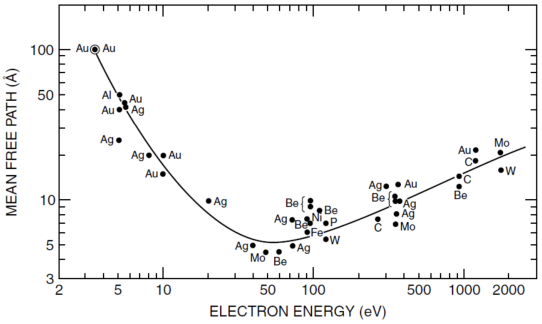

Figure 2: Escape depth curve. XPS results very surface sensitive in the range $20\,\text{eV} - 100\,\text{eV}$. Picture taken from [6]

- **Shake-up** process: due to the interaction with the core level photoelectron, a valence electron is excited to higher energy level. This corresponds to a secondary peak with energy slightly lower than that of the main peak.
- **Shake-off** process: after the emission of the core level photoelectron, a valence electron is ejected from the ion towards the continuum. This effect may lead to a broadening of the main peak or may contribute to the inelastic background region.

Since the energy of the photon emitted as a result of electron relaxation does not depend on the energy of the X-ray, the position of the peaks associated with Auger processes does not depend on the X-ray source used for the measurement. In contrast, the position of the peaks associated with all other processes depends directly on the energy of the photoelectron and thus on the X-ray source used.

2.4 Pick split

Another important effect we need to consider is the formation of multiplet structure. This can can be due to different effects:

- **Spin-orbit coupling**: this effect is due to the interaction between orbital angular momentum l and spin angular momentum s of the electron. The interaction can be described by the Hamiltonian
$$H_{so} = a\boldsymbol{S} \cdot \boldsymbol{L}$$
This effect divides the ground state into a doublet with $(l+1/2)$ and $(l-1/2)$. The s state does not exhibit the split, because the orbital angular momentum is 0.
- **Magnetic spin-spin exchange splitting**: effect due to the coupling between a complete s-shell and the magnetic spin moment associated to a non filled shell. This interaction can produce an energy splitting of the s-shell

2.5 Line width

Furthermore, another effect that need to be considered in the spectra produced by XPS is the **line width**. This can be simply described as

$$\Gamma^{tot} = \Gamma_0 + \Gamma^{noisy},$$

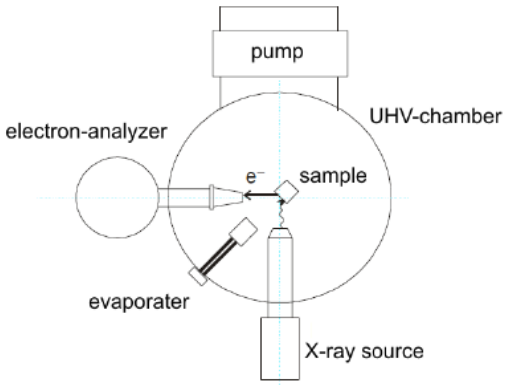

Figure 3: Schematic representation of the experimental setup. Picture taken from [1]

where Γ_0 is the irreducible line width and Γ^{noisy} is due to several noisy effects, such as the width of the exciting X-ray line, the energy resolution of the electron energy analyzer, and thermal broadening by interaction with phonons [1].

The irreducible line width Γ_0 is due to the Heisenberg uncertainty principle

$$\Delta E \Delta t \geq \frac{\hbar}{2}$$

where $\hbar$ is the Planck constant divided by 2π and ΔE, Δt are the uncertainties associated to the energy and to the time.

Since the lifetime τ of the state produced by the emission of the photoelectron is not infinite, according to the uncertainty principle the energy associated to the process will not have a specific value but a distribution. In particular the energy results distributed according to a Breigt-Wigner distribution and its width in corresponds approximately to

$$\Gamma \simeq \frac{\hbar}{\tau}.$$

3 Setup

The experiment consists, among other things, of a UHV chamber, an X-ray source, an evaporator and an electron analyzer. Figure 3 shows a schematic structure for the chamber. First, a cathode is used as an X-ray source. These emitted thermal electrons by heating up the filament. These electrons are accelerated by an anode. One can choose between aluminum and magnesium for the anode. This results in different wavelengths for the X-rays. The spectrum is measured with a hemispherical analyzer and a channeltron. With the help of the hemispherical analyzer, electrons with low energy can be filtered out to reduce noise.

3.1 UHV

A turbo molecular pump and an upstream rotary vane pump are used for the UHV chamber. First, the chamber is pumped out with the help of the rotary vane pump, since this generates a pressure range between 1 bar and 10^{-3} mbar. Then the turbo molecular pump is used to generate

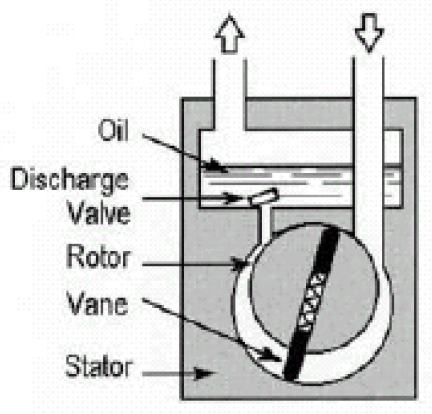

Figure 4: schematic structure of a vane pump.[8]

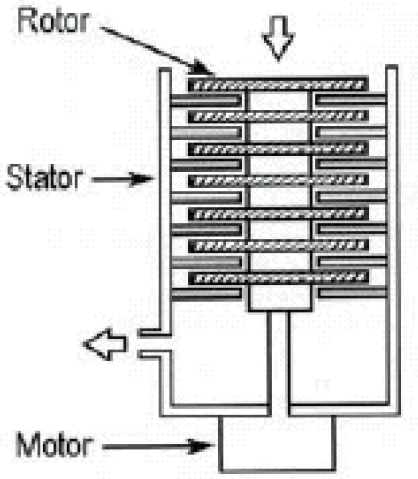

Figure 5: schematic structure of a turbomolecular pump. [8]

a pressure vin 10^{-9} mbar. Figure 5 shows a rotary vane pump. With the rotary vane pump, a vane pushes the molecule out of a valve. The turbomolecular pump is only able to pump heavy gases such as N_2, CO or N_2. Light gases such as H_2 or H_2 are not pumped out. In order for gases to be pumped out, the rotational speed of the rotator must be approximately the same as that of the gas. Gas molecules touching the rotator blade are accelerated. The atoms are kicked out of the chamber by the additional impulse. Only molecules that touch the underside of the rotor blades can be removed from the chamber. Molecules touching the rotator blades from above are reflected back into the chamber. With each contact there is a probability that the molecule will leave the chamber. Thus the pressure in the chamber decreases. Particles or molecules faster than the rotor blades will only collide from above. Because of this, these molecules cannot be pumped out. A turbo molecular pump rotates on average with 50×10^3 min With a radius of 10 cm, the speed for the rotator blades is about $500\,\mathrm{m\,s^{-1}}$. Molecule like H_2 which has a mean velocity of $1761\,\mathrm{m\,s^{-1}}$ or He with $1245\,\mathrm{m\,s^{-1}}$ cannot be removed with the turbo molecular pump. Under room conditions, water can bind to any metal surface. To remove this contamination, the chamber is baked once.[8][4][1]

3.2 X-ray source

As stated before a cathode is used to thermally emit electrons (usually with an intensity of 3 mA) which are then accelerated by the application of the voltage. This particular set up allows for the choice between two materials Mg and Al for the cathode.
Because the different elements have different characteristic radiations, changing the source allows us to probe different penetration lengths and energies which may be useful for example to distinguish Auger peaks from photoelectron peaks or to more closely analyze bulk or surface properties of the sample.
The figure 6 shows a setup for a twin anode X-ray source. Two cathodes and one anode are required for the Twin Anode X-ray source. On the tip of the anode is a silver substrate with a magnesium and an aluminum layer. Depending on which cathode is switched on, the electrons hit Mg or Al. The deflection of the electrons at Mg or Al results in bremsstrahlung. This radiation

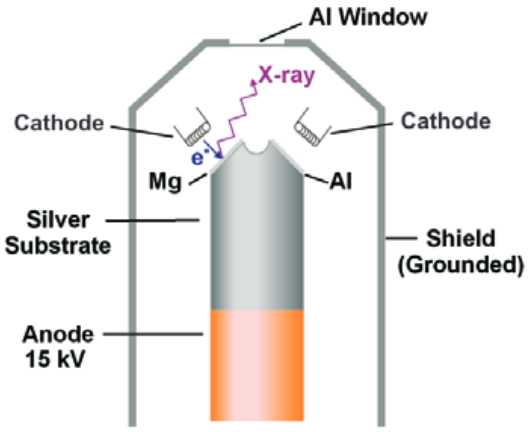

Figure 6: Schematic representation of the X-ray source. Picture taken from [5]

creates X-ray radiation. A shield with an Al window is located around the X-ray source. This ensures that the radiation flows through a point in a bundled form, weak radiation cannot escape through at all. This also ensures that the sample is not damaged. The chamber is completely locked to avoid any contamination.

3.3 Electron energy analyser

We use an electron energy analyzer which consists of a hemispherical capacitor to measure the kinetic energy of the photo-electrons. In addition, this set up allows for the use of a pass voltage E_{pas} so the less energetic secondary electrons are filtered out and thus the noise reduced.

Finally an structure consistent of a glass tube covered with a material with high electric resistance called a channeltron is used in conjunction with the corresponding electronics to amplify and detect the electrons.

3.4 Evaporator

The evaporator consists of a crucible and a filament wrapped around the crucible. The crucible is made of tantalum and inside the crucible is Sm. By heating the crucible, the Sm is evaporated.

4 Task

4.1 Measurement of Ag

In the first part we use the Al anode to measure the 3p and 3d orbital for Ag. The Ag sample was cleaned with a steel brush in the UHV. The pass energy was set to 50 eV to measure the full spectrum from 200 eV-1500 eV. After we located the peaks for the 3d and 3p orbital, we change the range at 1100 eV-1130 eV and pass energy of 30 eV. In this range we measure the 3d orbital for seven scan rates. Then we used the range from 870 eV-930 eV to measure the 3p orbital. Once the measurement of orbital 3d and 3p is compled, the range is set at 1450 eV-1500 eV and the pass energy at 50 eV. In this range the fermilevel is measured. Afterwards the

3p, 3d and fermilevel is measured again for the Mg anode. The full spectrum is measured in a range of 200 eV-1300 eV and a energy pass of 50 eV. The 3d orbital had a range of 840 eV-920 eV and energy pass of 30 eV. For the 3p orbital the range was 630 eV-710 eV. The range for the fermilevel was 1230 eV-1270 eV.

4.2 Measurement of Sm

After the measurement for Ag, the sample was changed to Sm. For this, Sm was evaporated to the sample. It is important that the electron energy analyser and the X-ray source is closed as long Sm is evaporated. Next the Al anode was used to measure the 3d orbital with an enegry pass of 30 eV and 50 eV. As range 360 eV-440 eV was used.

4.3 Measurement of DM

In the last measurement, the full spectrum for a DM was measured. For this, both the Mg anode and Al anode was used.

5 Analysis and protocol

5.1 Spectra of Ag metal

For the *Ag* sample we will use both a magnesium and aluminum light. In order to show the full spectra with respect to the binding energy we must first locate the Fermi edge as the value of the energy of the Fermi Level for the material will correspond to that of the work function. Recall that one can consider the Fermi Energy of a material as the energy needed to introduce one electron into it.

We search for the Fermi Edge at around the characteristic X-ray energy of aluminum and magnesium anodes respectively. We use a higher pass voltage of 50V for this inspection thus trading intensity for a lower resolution. This exchange is nevertheless prefered in this case as the electron count around the Fermi edge is typically low.

The obtained data are fitted using the *python* package *PyArpes* [7] to a Fermi-Dirac curve as seen in Fig. 7. Indeed the Fermi energies that we obtain are within the order of literature results as seen in Tab. 1, however they are not very precise as the data that gathered in the Fermi edge does not have a high resolution and the counts are relatively low.

Table 1: Values of the Fermi energy, that is the characteristic X-ray energy from the anodes minus the value of the material's Fermi level.

Anode	Us (eV)	Literature (eV) [2]
Al	(8.98 ± 0.51)	11.7
Mg	(9.6 ± 7.2)	7.08

In any case we use the obtained work functions to plot the binding energies as seen in Fig.8, here we have identified both 3p and 3d peaks, auger sequence peaks and also a 1s carbon peak possibly formed through deposition in the sample. Using two different materials for the anodes

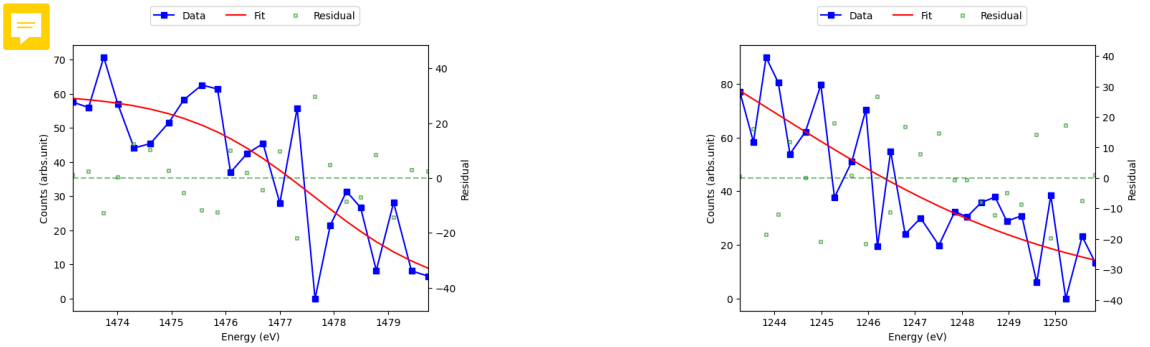

(a) Fermi edge for silver using Al source.

(b) Fermi edge for silver using Mg source.

Figure 7: Fermi edge area for both metals with a Dirac-Fermi curve fit, the residuals are shown in green. The Fermi level for the material is taken as the middle point of the curve which is part of the fitting parameters.

lets us compare the plots for both the kinnetic energy and the binding energy in order to distinguish the features of XPS.

Crucially because the binding energy of the orbitals does only depend on the structure of the atom these will appear aligned in the binding energy plot for both anode materials. Meanwhile properties that do not depend on the atoms structure but on the environment and material such as Auger Peaks will appear aligned in the kinetic energy plot while shifted when shown with respect to binding energy. This lets us identify a set of characteristic Auger peaks in the low KE.

We show the results obtained for the binding energies of the various peaks in table 2. The binding energies obtained although within a reasonable range are constantly underestimated. One possibility is that errors in the identification of the work functions will affect the computed binding energies also the binding energy of the orbitals in bulk, contamination of the sample can also induce chemical shifts of the binding energy while the orbital energies in bulk will tend to be lower than for a single atom due to neighbouring interactions.

While the 1s binding energy has been computed by simply taking the position of the maximum of the peak in the full spectra, closer inspection has been used to analyze the binding energies of the silver orbitals. In that case we have analyzed a region around said peaks using a lower pass voltage of 30V such that less noisy electrons will be detected and we would be able to obtain a higher resolution. In both cases we observe an splitting of the orbitals due to spin-coupling interactions leading to the creation of two separate peaks for both degenerate states $3p_{1/2}$,$3p_{3/2}$ and $3d_{3/2}$,$3d_{5/2}$.

The peaks have been fitted using Gaussian functions through the *PyArpes* package and are shown in Fig. 9 where we can see how in general the 3d peaks are better defined than the 3p due to the difference in electron count being higher in the former. For this reason the region between the 3p peaks appears to be more noisy, even generating a false peak for the case with the Aluminum anode.

Table 2: XPS orbital peaks deteced in the Ag sample. The high energy peaks can be identified with the 3p and 3d orbitals of silver, while the lowest binding energy peak can be identified as a carbon 1s possible deposited through CO_2.

Orbital	Element	Us (Al) (eV)	Us (Mg) (eV)	Literature (eV) [1]
1s	C	(279.66 ± 0.71)	(275.9 ± 7.2)	284.2
$3p_{3/2}$	Ag	(362.36 ± 0.51)	(358.5 ± 7.2)	368.3
$3p_{1/2}$	Ag	(368.07 ± 0.51)	(364.5 ± 7.2)	374.0
$3d_{5/2}$	Ag	(565.60 ± 0.51)	(560.4 ± 7.2)	573.0
$3d_{3/2}$	Ag	(594.45 ± 0.53)	(591.1 ± 7.2)	603.8

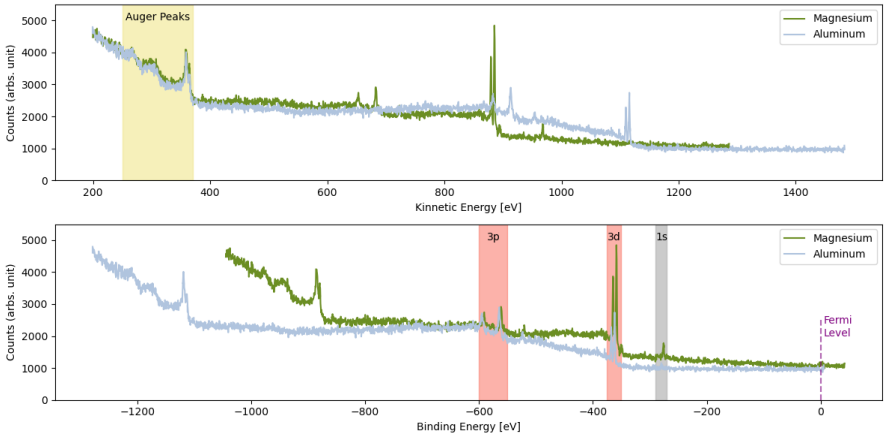

Figure 8: Plots showing the obtained XPS spectra both with respect to the measured kinnetic energy of the electrons (above) and the binding energy (below) for both kinds of anodes with the Ag sample. The salmon shaded areas areas show the peaks identified as pertaining to Ag orbitals while the gray shaded area represents a Carbon orbital. Note that peaks that features that depend only on the structure of the atoms (orbital peaks) appear aligned in the binding energy plot while features that depend on the environment (Auger Peaks) appear aligned in the KE one.

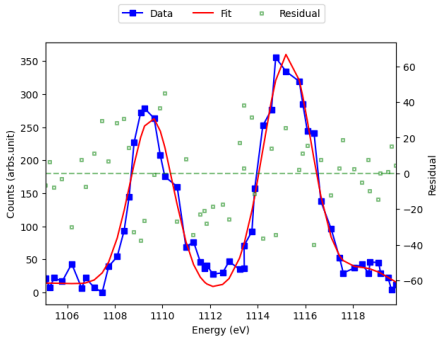

(a) $3d_{1/2}$ peak on the left and $3d_{3/2}$ peak on the left for Ag with Al source.

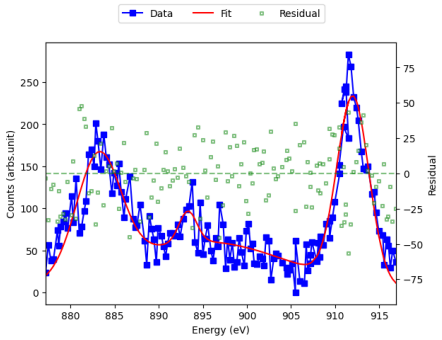

(b) $3p_{3/2}$ peak on the left and $3p_{5/2}$ peak on the left for Ag with Al source.

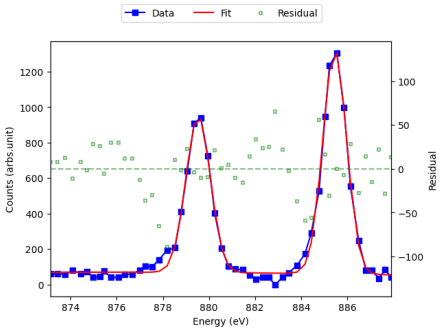

(c) $3d_{1/2}$ peak on the left and $3d_{3/2}$ peak on the left for Ag with Mg source.

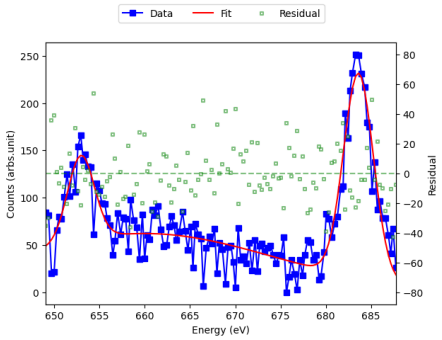

(d) $3p_{3/2}$ peak on the left and $3p_{5/2}$ peak on the left for Ag with Mg source.

Figure 9: XPS peaks for Ag with both available anodes. The peaks have been fitted using Gaussian functions through the *PyArpes* package. The fit is showed in red, while in blue we show the data points and the residuals of the fit. The peaks are shown with respect to KE.

5.2 Spectra of Sm Metal

Next we change our sample to a thin layer of Samarium which we evaporate thanks to the heat from a filament. Again we start by taking the full spectra with a pass voltage of 50V and we use both anodes in order to properly identify the peaks.

Again we show both the XPS peaks in regards to the binding energy and the kinetic energy in Fig. 10. In the one regarding KE one can observe a possible Auger sequence when the two plots align. While the plot in relation to binding energy lets us identify the areas where the main 3d and 4p peaks of Sm will be found. Again we also detect a 1s peak resulting of sample contamination, however this time the energy signature is that of an oxygen atom - which indicates that our sample might be oxidized.

The binding energies for the detected peaks are shown in table 3 where the peaks for 1s carbon and 4s samarium have been obtained from the full spectra in the same way as for the oxygen in silver. Not surprisingly this peaks deviate more from the literature values than the ones where a committed scan with XPS was done. Indeed the low resolution of the full spectra did not permit the detection of the 4p splitting.

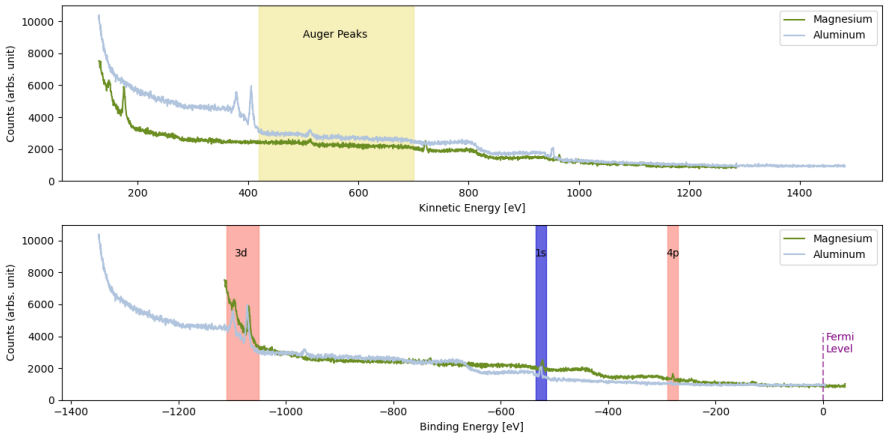

Figure 10: Plots showing the obtained XPS spectra both with respect to the measured kinnetic energy of the electrons (above) and the binding energy (below) for both kinds of anodes with the Sm sample. The salmon shaded areas areas show the peaks identified as pertaining to Sm orbitals while the gray shaded area represents an Oxygen orbital.

Regarding the 3d peaks, the splitting is obvious in both the full spectra and the focused spectra. Like for the case of silver the range of energies where the peaks showed in the full spectra was analyzed more thoroughly in order to obtain more detailed data. However in this case only the aluminum anode was used as the magnesium would not have had the necessary energy as is made apparent in Fig. 10.

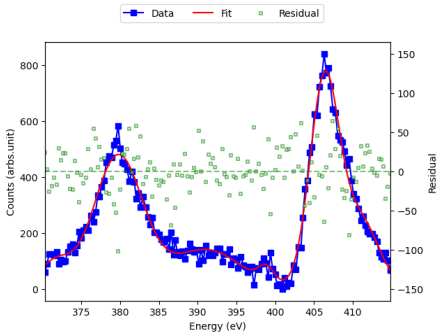

(a) $3d_{1/2}$ peak on the left and $3d_{3/2}$ peak on the left for Sm with Al source at 30V.

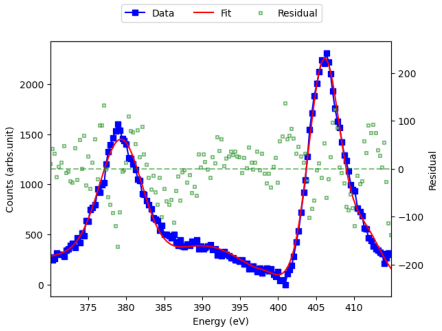

(b) $3d_{1/2}$ peak on the left and $3d_{3/2}$ peak on the left for Sm with Al source at 50V.

Figure 11: XPS peaks for Sm with both possible values for the voltage pass. The peaks have been fitted using Gaussian functions through the *PyArpes* package. The fit is showed in red, while in blue we show the data points and the residuals of the fit. The peaks are shown with respect to KE.

On the other hand the pass energy was changed and Gaussian fits were produced in both cases. These are shown in Fig. 11 where we can see that in this case the resolution seems to be

Table 3: Binding energies of the XPS peaks detected on the Sm sample. The asterisk for the value of 4p indicates that this is the mean of the two split orbitals.

Orbital	Pass Voltage (V)	Element	Us(Al) (eV)	Us(Mg) (eV)	Literature (eV) [1]
1s	50	O	524.44 ± 0.75	522.1 ± 7.2	543.1
4p	50	Sm	283.35 ± 0.75	279.6 ± 7.2	256.5*
$3d_{5/2}$	50	Sm	1071.59 ± 0.53	–	1083.4
$3d_{5/2}$	30	Sm	1071.25 ± 0.53	–	1083.4
$3d_{3/2}$	50	Sm	1098.48 ± 0.52	–	1110.9
$3d_{3/2}$	30	Sm	1097.89 ± 0.52	–	1110.9

slightly better for the 50V pass energy than for the 30V. However with more exposure time the low pass should become less noisy and more defined than the high pass results.

Regarding the position of the peaks in both cases they are quite similar and both below the literature results. Again this may be due to chemical shifts - as we have detected oxygen in the sample - as well as the fact that the electrons will loose some amount of kinetic energy until they are detected.

Finally we compute the coupling constant for the various electronic shells of both samarium and silver, using the relation

$$a = \frac{2\Delta E}{5\hbar^2},$$

where ΔE is the weight of the pick, for the 3d picks, and

$$a = \frac{2\Delta E}{3\hbar^2},$$

for the 3p picks. On table 4 we see that the coupling constant is consistent for the same orbitals of the same element and that Samarium's 3d orbital has a stronger coupling constant than for silver possibly due to the more complex electronic structure and number of shells in the latter. Similarly the 3p orbital's coupling constant is quite higher than that of 3d's for silver, again this may be due to the interactions of the electrons with the other orbitals and given that 3p orbital is closer to the core it would be reasonable to expect a stronger interaction. Moreover the 3p orbital is less localized than the 3d orbital which also implies a higher overlap with neighbouring electrons.

Table 4: Coupling constants for Ag and Sm orbitals.

Orbital	Element	Anode	Pass Voltage (V)	Coupling Constant ($eV \cdot s^2$)
3d	Ag	Al	30	2.28 ± 0.29
3d	Ag	Mg	30	2.4 ± 4.1
3p	Ag	Al	30	19.23 ± 0.49
3p	Ag	Mg	30	20.5 ± 6.8
3d	Sm	Al	30	10.65 ± 0.30
3d	Sm	Al	50	10.76 ± 0.29

5.3 Spectra of the Coin

In the last task we analyzed the spectrum of a 10-DM coin. The spectrum obtained using Aluminium as X-ray source is shown in Fig. 12, while the spectrum obtained using Magnesium as source is shown in Fig. 13. For both spectra, the binding energy is obtained subtracting the kinetic energy measured in correspondence of the Fermi level, that was obtained from the fit in the previous tasks. Both spectra present peaks corresponding to $2p1/2$ and $2p3/2$ copper, $1s$ oxygen, $1s$ carbon and $4s$, $2p_{3/2}$, $2p_{3/2}$ of Sm . In Aluminium spectrum is also visible the $2s$ peak of Cu and $2d_{5/2}$, $2d_{3/2}$ peaks of Sm.

From the values in table 5 we can observe that the peak values present a negative shift respect to the reference value. This can be due to some factors like an error in the estimate of the work function, the sensibility of the instruments, chemical shifts due to mixed compositions of the sample and the loss in innetic energy that an electron experiences until it is detected.

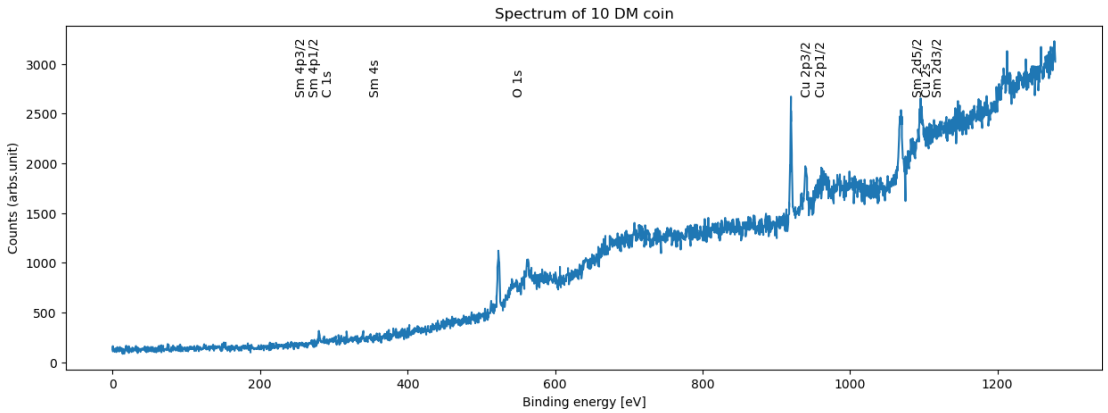

Figure 12: In the graph is reported the 10-DM coin's spectrum, obtained using Al as X-ray source

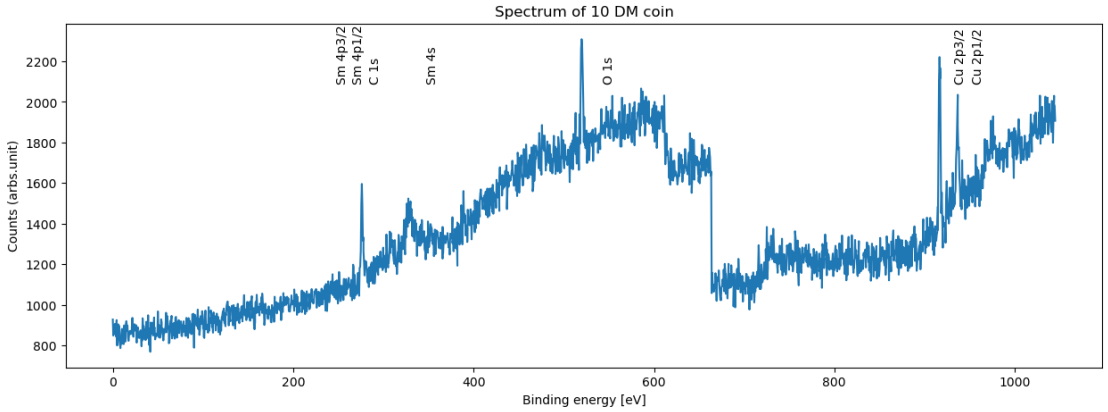

Figure 13: In the graph is reported the 10-DM coin's spectrum, obtained using Mg as X-ray source

Table 5: XPS orbital peaks detected in the 10-DM coin. In the coin are present peaks associated with carbon, oxigen, cooper.

Orbital	Element	Us (Al) (eV)	Us (Mg) (eV)	Literature (eV)
1s	C	(279.9 ± 1.9)	(276 ± 8)	284.2
1s	O	(523 ± 2)	(520 ± 9)	543.1
$2p_{3/2}$	Cu	(920.1 ± 1.9)	(917 ± 8)	932.7
$2p_{1/2}$	Cu	(940 ± 2)	(936 ± 9)	952.3
2s	Cu	(1084 ± 6)	-	1096.7
$2d_5/2$	Sm	(1068 ± 3)	-	1083.4
$2d_3/2$	Sm	(1095 ± 3)	-	1110.9
4s	Sm	(339.6 ± 1.2)	(341 ± 9)	347.2
$4p_{1/2}$	Sm	(239 ± 14)	(343 ± 15)	265.6
$4p_{3/2}$	Sm	(209 ± 7)	(210 ± 11)	247.6

6 Error discussion

When considering error analysis for XPS, several aspects must be considered. The first is the surface of the sample. Since the photoelectrons can mainly only penetrate a few layers, any contamination on the surface makes a big difference. If, for example, oxygen binds to the surface, the chemical shift can change. This can change the energy of the orbitals.

Another problem is surface degradation over time. The lattice structure can change over time due to the photoelectrons. The surface of the sample is destroyed in the process. The destruction of the surface can change the work function for the exit energy.

XPS analyzes only the top few nanometers of the material, so any variation in surface conditions, such as surface roughness or non-uniform composition, can affect the results. It is essential to consider the surface preparation and handling of the sample to minimize such effects, ideally one should make sure that surface stays clean and polished both before and during the experiment.

Another problem is the charging effect of the material. When the electrons leave the sample, individual atoms are positively charged for a short time. Due to this charge change, the energy for the orbitals can change very slightly. Since electrons can move very quickly in metals, the missing charge is compensated for in a short time.

Finally, errors can arise due to variations in instrumental parameters, such as X-ray beam spot size, sensitivity factors, and detection efficiency or energy loss of the electron until detection. Careful calibration and standardization procedures are necessary to minimize these errors.

7 Conclusions

Overall we have been able to identify the signature peaks of the 3p and 3d orbitals of our samples within a reasonable accuracy. Moreover we have been able to identify unknown elements, which is useful for both determining possible sources of contamination on the surface - as seen with carbon and oxygen for Ag and Sm - as well as gauging the composition of thin objects such as it was with the case of the Deutsche Mark coin.

Typically the measured peaks have shown to have smaller energies than those reported by literature provided in [1]. Possible causes for this disagreement include changes in the electronic structure after the electron leaves the orbital, loses of energy due to the electron having to travel to the detector or propagation of errors from when the work function was computed. In fact we have been able to estimate the work function through observation of the Fermi edge, where our results even though less satisfactory than those of the binding energies stay within the order of the literature.

Regarding peak identification, we have also check the importance of having multiple anodes and plotting the spectra in both the kinetic and binding energy plots; as this allows us to distinguish the orbital peaks (which align in the binding energy plot) from signals that do not depend on the binding energies of the atoms (as Auger peaks). Also we have been able to change the pass energy of the detector which is reflected on the resolution and number of counts detected.

Finally we have also been able to observe the splitting of 3p and 3d orbitals and the lack of it in s type orbitals as expected. Indeed we ahve also computed the spin-orbit coupling constants for the p and d-orbitals obtaining in general higher coupling constants for the p-orbitals. We believe this may be due to the shape of the p-orbitals allowing the electrons to overlap with other electronic structures of the atom as well as it being spatially closer to the core. In a similar vein we have also obtained a higher coupling constant for 3d in the case of the heavier samarium atom. We think that this may be due to interaction with more electronic shells.

Overall we have been able to use the XPS techinque to both study and identify the electronic configuration of the sample's surfaces.

References

[1] X-ray photoelectron spectroscopy (xps). 17:1–17, 2011.

[2] T. Alford, L. Feldman, and J. Mayer. *Fundamentals of nanoscale film analysis*. Springer US, 2007. Copyright: Copyright 2014 Elsevier B.V., All rights reserved.

[3] S. Hüfner. *Photoelectron spectroscopy: principles and applications*. Springer Science & Business Media, 2013.

[4] Leybold. How doeas a turbomolecular pump work. *Leybold*.

[5] T. F. Scientific. Xr3: Twin anode x-ray source. *Thermo Fisher Scientific*, 1:1–4, 2008.

[6] G. Somorjai. *Chemistry in Two Dimensions: Surfaces*. Cornell Paperbacks. Cornell University Press, 1981.

[7] C. Stansbury and A. Lanzara. Pyarpes: An analysis framework for multimodal angle-resolved photoemission spectroscopies. *SoftwareX*, 11:100472, 2020.

[8] M. Weinelt. Surface science. *Zeitschrift für physik*, 1:9–12, 2023.